Highly scalable multichannel mesh electronics for stable chronic brain electrophysiology

Highly scalable multichannel mesh electronics for stable chronic brain electrophysiology

Tian-Ming Fu[a,1], Guosong Hong[a,1], Robert D. Viveros[b], Tao Zhou[a], and Charles M. Lieber[a,b,2]

[a]Department of Chemistry and Chemical Biology, Harvard University, Cambridge, MA 02138; and [b]John A. Paulson School of Engineering and Applied Sciences, Harvard University, Cambridge, MA 02138

Contributed by Charles M. Lieber, October 19, 2017 (sent for review October 10, 2017; reviewed by Dae-Hyeong Kim and Bozhi Tian)

Implantable electrical probes have led to advances in neuroscience, brain–machine interfaces, and treatment of neurological diseases, yet they remain limited in several key aspects. Ideally, an electrical probe should be capable of recording from large numbers of neurons across multiple local circuits and, importantly, allow stable tracking of the evolution of these neurons over the entire course of study. Silicon probes based on microfabrication can yield large-scale, high-density recording but face challenges of chronic gliosis and instability due to mechanical and structural mismatch with the brain. Ultraflexible mesh electronics, on the other hand, have demonstrated negligible chronic immune response and stable long-term brain monitoring at single-neuron level, although, to date, it has been limited to 16 channels. Here, we present a scalable scheme for highly multiplexed mesh electronics probes to bridge the gap between scalability and flexibility, where 32 to 128 channels per probe were implemented while the crucial brain-like structure and mechanics were maintained. Combining this mesh design with multisite injection, we demonstrate stable 128-channel local field potential and single-unit recordings from multiple brain regions in awake restrained mice over 4 mo. In addition, the newly integrated mesh is used to validate stable chronic recordings in freely behaving mice. This scalable scheme for mesh electronics together with demonstrated long-term stability represent important progress toward the realization of ideal implantable electrical probes allowing for mapping and tracking single-neuron level circuit changes associated with learning, aging, and neurodegenerative diseases.

ultraflexible | tissue-like | neural probe | large-scale neural recording | nano–bio interface

Implantable electrical probes comprising electrodes capable of recording and stimulating brain activity have proven to be critical tools to decipher how information is encoded inside the brain (1–4), to treat chronic neurological diseases, including Parkinson's diseases (5–7), and to realize brain–machine interfaces (BMIs) (8–11). In contrast to electroencephalography surface probes (12, 13) and noninvasive brain imaging methods, such as functional magnetic resonance imaging (14), implantable electrical probes can offer spatiotemporal mapping at the single-neuron level by positioning sensing units in close proximity to individual neurons comprising local neural circuits of interest (1). In addition, implantable electrical probes can access virtually any brain region from freely behaving subjects without issues of optical penetration depth, acquisition rates, and incorporation of fluorescent labels, which can compromise the single-neuron resolution and large-scale circuit mapping capability of optical imaging techniques (15, 16).

A key goal of implantable electrical probe development is to realize stable single-neuron-level high-density brain mapping over long time periods. High-density recording of local circuit activity consisting of large numbers of neurons combined with large-scale correlation across multiple interconnected brain regions could offer insight into how the brain processes information from locally connected microcircuits to long-range correlated macronetworks (17–19). In addition, stable tracking of these targeted neurons and neural circuits over time could illuminate how the brain gradually evolves during development, learning, memory, and disease progression (7, 20–22). For example, studies of the memory engram, which is believed to comprise widely distributed networks of neuron ensembles with changes at single-neuron level long after encoding, present a particular challenge for current techniques in terms of recording stability and the number of channels; that is, it is difficult to track the time evolution of the same distributed networks of neurons constituting an engram to reveal the distributed and dynamic nature of memory representations in the brain (21). Similarly, the capability to simultaneously track and interact with a large number of the same neurons on an individual basis with a stable long-term interface could enable accurate and deterministic BMI control for restoration of lost neural functions, a crucial challenge faced by existing intracortical electrode arrays (9, 10). In this context, ideal implantable electrical probes with single-neuron-level spatiotemporal resolution, multiple brain region coverage, and, critically, stable tracking of the time evolution of these behavior-related neurons and neural circuits could significantly advance the understanding of brain computation and treatment of neurological and neurodegenerative diseases.

Important progress has been made toward improving implantable electrical probes. Advancements in microfabrication processes and circuit design have significantly increased the number of recording channels in a single probe and the number

Significance

Implantable electrical probes have led to fundamental neuroscience advances and treatment of neurological diseases, yet are unable to stably track the long-term evolution of large numbers of individual neurons critical to brain functions. Here, we demonstrate a scalable scheme for highly multiplexed mesh electronics probes that overcomes this long-standing challenge. We illustrate this scheme through fabrication of 32 to 128 channel probes with macroporous neural network-like structure and flexibility comparable to the brain. Following implantation into rodent brains, we demonstrate chronic 128-channel recordings with single-neuron-level stability from multiple brain regions over 4 mo. These scalable mesh electronics probes represent an ideal platform for mapping, tracking, and modulating the single-neuron-level circuit changes associated with learning, aging, and neurodegenerative diseases.

Author contributions: T.-M.F., G.H., and C.M.L. designed research; T.-M.F., G.H., R.D.V., and T.Z. performed research; T.-M.F., G.H., and C.M.L. analyzed data; T.-M.F., G.H., and C.M.L. wrote the paper; and R.D.V. and T.Z. discussed results and manuscript.

Reviewers: D.-H.K., Seoul National University; and B.T., The University of Chicago.

The authors declare no conflict of interest.

[1]T.-M.F. and G.H. contributed equally to this work.

[2]To whom correspondence should be addressed. Email: cml@cmliris.harvard.edu.

This article contains supporting information online at www.pnas.org/lookup/suppl/doi:10.1073/pnas.1717695114/-/DCSupplemental.

of implanted probes in the same object (17–19, 23, 24). For example, silicon-based Michigan array probes comprising eight 128-channel shanks capable of targeting four spatially distinct neuroanatomical planes and recording both local field potentials (LFPs) and single-unit spikes from 1,024 electrodes have been reported (19). More recently, a single-shank silicon probe containing 384 channels with 966 switchable recording sites has been tested (25) (Harris TD, et al. Neuroscience Meeting Planner, November 12–16, 2016, San Diego, CA.). While these improvements leveraging advances in microfabrication allow for highly scalable probes, they do not overcome the existing limitations of such rigid probes, including relative shear motion, which leads to signal instability, and a chronic immune response producing glial scarring, which depletes neurons surrounding the probes and causes signal degradation over a time scale of weeks (26–30). Together, these limitations hinder fundamental neuroscience studies and clinical applications.

On the other hand, we have recently reported a paradigm for implantable electrical probes termed mesh electronics, where the implant is designed with a macroporous structure, brain-like ultraflexibility, and feature sizes smaller than neuron soma (31–34). Recent studies have shown that implanted mesh electronics can yield seamless 3D integration with the endogenous neuronal network without chronic gliosis (31, 33–35), and allow for stable tracking of the same individual neurons on a months-to-year time scale without probe repositioning (33). A central challenge faced by mesh electronics development is its scalability on the number and density of independently addressable channels. Specifically, while additional channels could be easily incorporated into the mesh probes by increasing the density of longitudinal elements, this would also diminish the unique advantage brought by the macroporous structure and ultraflexible mechanics of the mesh for brain interface; a large unit-cell opening with bending stiffness comparable to that of the brain is essential for achieving seamless integration and interpenetration with neural networks, negligible chronic gliosis, and minimum relative shear motion (33, 34). Therefore, a scalable scheme that could significantly increase the number and density of channels for individual mesh probes while maintaining the macroporous and ultraflexible characteristics of previous low-channel mesh designs is critical for broader applications of mesh electronics, where stable long-term tracking of large numbers of neurons at the single-neuron level could impact substantially fundamental neuroscience and neurological therapeutics.

Herein, we introduce a jump forward in the mesh electronics concept with a scalable scheme to achieve highly multiplexed mesh probes, and demonstrate this scheme with mesh electronics probes containing 32 to 128 recording sites per probe and maintaining critical brain-like ultraflexibility and minimal electrical cross-talk between channels. Using these scalable mesh probes, we further show simultaneous 128-channel chronic electrophysiological recordings from distinct mouse brain regions with stable single-unit spikes waveforms, clustering, and firing rates in the majority of recording electrodes for at least 4 mo.

Results

Design of Scalable Highly Multiplexed Mesh Electronics. Our central aim for the highly multiplexed mesh electronics design is to implement a scalable scheme to increase the number and density of recording sites while maintaining the crucial brain-like mechanics and structure. Schematically, we achieved this goal via implementation of the approach outlined in Fig. 1 *A* and *B*. The overall base mesh structure (Fig. 1*A*) contains 32 longitudinal elements, where scaling in channel number is readily achieved by incorporating two or more independent metal interconnect lines per longitudinal element. For example, the case of two interconnects per longitudinal element is highlighted in Fig. 1*A*, *Inset*. Importantly, unlike all previous examples of mesh structures used for tissue engineering (36–38) and neural probes (31–35)

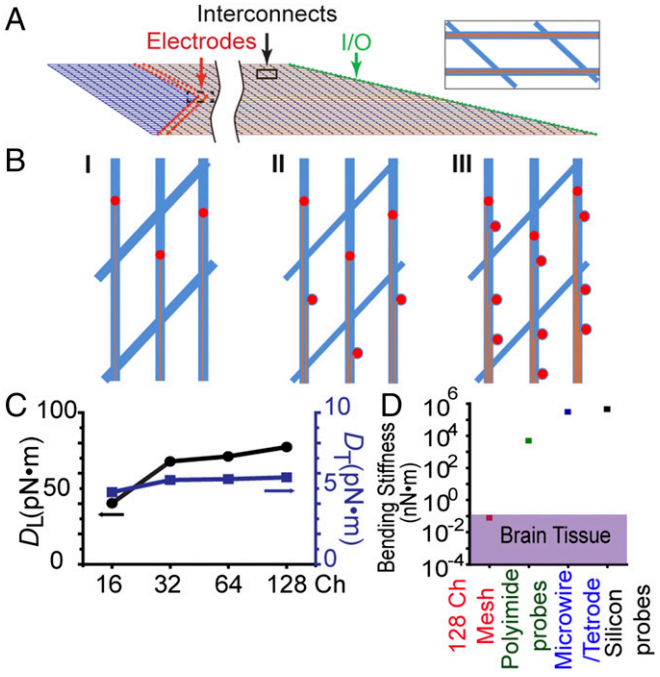

Fig. 1. Scalable scheme for high-density multiplexed mesh electronics. (*A*) Scheme showing a 64-channel scalable highly multiplexed mesh electronics probe with 32 longitudinal elements. Two individually addressable metal interconnects (orange lines) are incorporated in each longitudinal element (*Inset*) connecting recording electrodes (red circles) at one end and I/O pads (green circles) at the other end. The dashed and solid black boxes highlight the electrodes and interconnects region shown in *B*, *II* (rotated 90°) and *Inset*, respectively. (*B*) Schematics showing scaling of channel number and recording site density via incorporation of multiple channels in a single longitudinal element. Red circles, orange lines, and blue mesh structures represent the Pt microelectrodes, Au interconnects, and SU-8 mesh ribbons, respectively. (*C*) Simulated longitudinal (black, left *y* axis) and transverse (blue, right *y* axis) bending stiffness values for the 16-, 32-, 64-, and 128-channel mesh designs. The 16-channel mesh has the same structure as reported previously (33) (see *Materials and Methods* and *SI Text* for simulation details). (*D*) Comparison of the bending stiffness of 128-channel mesh electronics (red square) with that of brain tissue (purple rectangle) and those of conventional implantable electrical probes: planar polyimide probes (39) (green square), microwire or tetrode (18) (blue square), and silicon probes (black square) (40).

that were limited to one interconnect line per longitudinal element, the incorporation of multiple lines on each longitudinal element allows for significant increases in the total number of recording channels on a single probe while maintaining the unique neuronal-scale dimensions and mesh openings larger than the sizes of neuron somata and other cells reported (31–35) to facilitate healing and integration of neural tissue with the mesh postimplantation.

Each interconnect line terminates and addresses an independent microelectrode such that the cases of one, two, and four interconnects per longitudinal element yielded one, two, and four recording electrodes (red circles, Fig. 1*B*) per longitudinal element and 32, 64, and 128 recording channels per mesh electronics probe, respectively. As shown in Fig. 1*B*, the recording electrodes on the same longitudinal elements of the 64- and 128-channel designs were displaced both vertically and horizontally to avoid overlap with the interconnect lines, where the horizontally displaced electrodes (lower portion, Fig. 1 *B*, *II* and *III*) were closer to the input/output (I/O) connections indicated in Fig. 1*A* (green circles).

We carried out finite element simulations to evaluate the mechanical properties of the scalable mesh electronics designs, and, in particular, to quantify the longitudinal (D_L) and transverse (D_T)

bending stiffness values (*Materials and Methods* and *SI Text*). A summary of the results for the 32-, 64-, and 128-channel scalable mesh electronics designs, as well as comparison with previous results for a 16-channel mesh probe (31, 33), are shown in Fig. 1*C* and highlight several points. First, the analysis shows that D_L and D_T for the base mesh structure with 32 longitudinal elements only increase ~2 and 1.1 times, respectively, compared with the previous 16-channel mesh probe (33). Second, it is important to note that there is almost no further increase in either D_L or D_T for the 64- and 128-channel mesh probes from their 32-channel counterpart, thus validating our design goal. The minimal change in these values on increasing from 32 to 128 channels reflects the very small contribution of the Au interconnects (100-nm thickness) to the overall mechanical properties of the mesh electronics. This minimal contribution from Au interconnects to the overall bending stiffness leaves substantial room for further increases in the number of channels that could be defined in a single longitudinal ribbon. In addition, the bending stiffness values of our scalable mesh probe design remains within the range expected for brain tissue (see *Materials and Methods* and *SI Text*), and is three to six orders of magnitude smaller than bending stiffness values of conventional implantable brain probes as compared in Fig. 1*D* (18, 33, 39, 40).

Fabrication and Characterization of 32- to 128-Channel Mesh Electronics. Highly multiplexed mesh electronics probes based on this scalable design were fabricated using standard photolithography (PL) procedures (32–36) (see *Materials and Methods*, *SI Text*, and Fig. S1). In these scalable mesh designs, the gold (Au) interconnect line widths were all 2 μm, with a separation of 8 μm and 2 μm for the 64- and 128-channel designs, respectively. Overall, our fabrication process includes four PL steps that are carried out following deposition of a nickel metal sacrificial layer on a 3-inch silicon wafer; these steps involve defining (*i*) the bottom polymer (SU-8) mesh structure, (*ii*) the Au metal interconnect lines and I/O pads, (*iii*) the Pt metal recording electrodes, and (*iv*) the top polymer mesh structure, which encapsulates the interconnect lines, leaving only the recording electrodes and I/O pads exposed. This approach allows for facile preparation of multiple scalable mesh electronics probes in a single fabrication run. For example, Fig. 2*A* shows 21 scalable mesh electronics probes, seven each of the 32-, 64-, and 128-channel designs, fabricated on a single 3-inch silicon wafer, which can be completed in 3 d to 4 d following design of the contact PL masks.

Bright-field optical microscopy images of individual 32-, 64-, and 128-channel mesh electronics probes before release from a fabrication substrate (Fig. 2*B*) highlight the overall similarity of these scalable probes based on the 32 longitudinal element design. In addition, comparison of higher resolution microscopy images of the 32-, 64-, and 128-channel mesh electronics (Fig. 2*C*) makes clear that the increase in recording channel number and density is achieved with the same porosity mesh structure. These images and zoom-in insets further highlight the one, two, and four 2-μm-wide Au interconnects per longitudinal element used in the 32-, 64-, and 128-channel probes, respectively, as well as the layout of the 20-μm-diameter Pt recording electrodes (red arrows) in each of the probes, where two and four electrodes per longitudinal element were displaced laterally to enable independent addressing in the 64- and 128-channel designs, respectively.

The ultraflexible nature of the highly multiplexed scalable mesh electronics is apparent following release from the fabrication wafer by etching of the sacrificial nickel metal layer (see *Materials and Methods* and *SI Text*). First, a photograph (Fig. 3*A*) and video (Movie S1) of seven 128-channel mesh electronics probes suspended in water show clearly their conformation flexibility, and, moreover, the video demonstrates the robustness of the mesh structure while "stirring" with a glass needle. Second, and crucial to in vivo applications, the 32-, 64-, and 128-channel mesh electronics can be loaded into and ejected from glass capillary

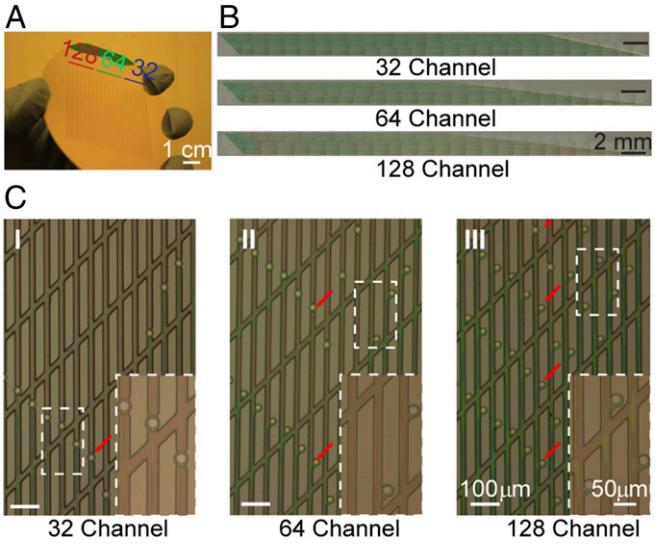

Fig. 2. High-density multiplexed mesh electronics via standard PL. (*A*) Photograph showing fabricated 32-, 64-, and 128-channel mesh designs on a 3-inch (76.2 mm) diameter silicon wafer before dissolution of the Ni sacrificial layer. A total of 21 mesh electronics probes with 7 of each channel design were fabricated on the wafer. (Scale bar: 1 cm.) (*B*) Stitched bright field microscope images showing fabricated 32- (*Upper*), 64- (*Middle*), and 128-channel (*Lower*) mesh electronics probes on a silicon wafer. Recording electrodes and I/O pads are located at the left and right, respectively, of the images. Each stitched image comprises *ca*. 50 wide-field microscope images (1.35 mm × 1.70 mm for each image) taken under 5× magnification. (Scale bars: 2 mm.) (*C*) Bright-field microscope images showing scaling up of channel number and recording site density via fabricating multiple (1, 2, and 4 in *I*, *II*, and *III*, respectively) channels in a single longitudinal element. The red arrows highlight the number of recording sites (Pt microelectrodes) on a single longitudinal element. *Insets* present zoom-in views of the white dashed boxes. [Scale bars: 100 μm and 50 μm (for *Inset*).]

needles in a manner similar to our reports for the 16-channel design (32, 33). For example, differential interference contrast (DIC) (Fig. 3*B*) and confocal fluorescence (Fig. 3*C*) microscopy images showed that the 128-channel mesh electronics probe could be loaded and ejected through a 400-μm inner diameter (ID) capillary without jamming or damaging the mesh integrity. In addition, confocal images (Fig. 3*C*, *Inset*) highlight the four independent interconnect lines insulated by SU-8 polymer in this 128-channel mesh electronics probe.

We have also investigated potential electrical cross-talk of the highly multiplexed scalable mesh electronics probes by assessing the frequency-dependent impedance between adjacent Au interconnects of a 128-channel mesh probe, which has the highest density of interconnects with a 2-μm edge-to-edge separation (see *Materials and Methods* and *SI Text*). Measurements made from 1 kHz to 10 kHz (red data, Fig. 3*D*), which are most relevant to single-unit spike recording, yield an average impedance of 2 GΩ to 3 GΩ and 0.2 GΩ to 0.3 GΩ at 1 and 10 kHz, respectively. Comparison with measurements of the Pt recording electrode impedance over the same frequency range (green data, Fig. 3*D*) shows that the electrode impedance is *ca*. four orders of magnitude smaller than the impedance between nearest interconnect lines. Furthermore, the resistance of the 2-μm interconnect line (*ca*. 4 kΩ) is two orders of magnitude smaller than that of the Pt recording electrode impedance and, therefore, introduces minimum perturbations to recorded signals. Importantly, these results demonstrate that there is minimal cross-talk for our highest-density 128-channel mesh electronics probes, and also suggest that it should be possible in the future

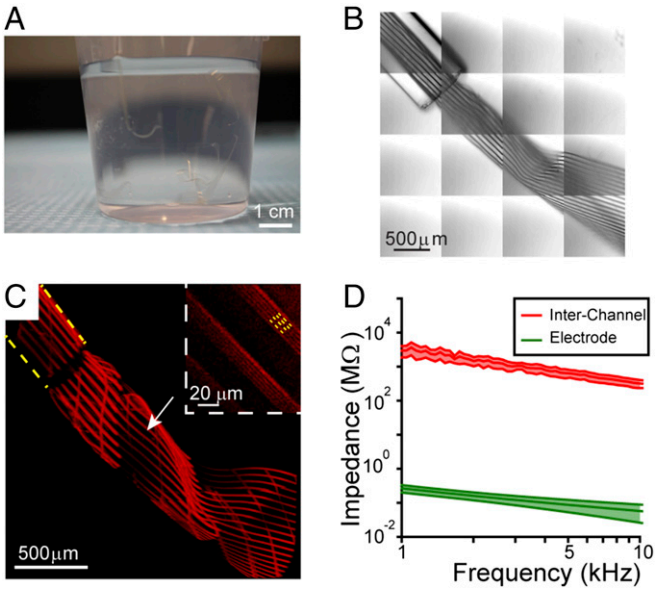

Fig. 3. Imaging and electrical characterization of highly multiplexed mesh electronics. (*A*) Photograph of seven free-standing 128-channel mesh electronics with the design shown in Fig. 2*C*, *III* suspended in water. The mesh electronics were transferred by glass needles after being released from the silicon wafer. (Scale bar: 1 cm.) (*B*) DIC image of a 128-channel mesh electronics injected through a 400-μm ID glass needle into water. The image was acquired in 4 × 4 Tile Scan mode with each of the tiles having a field of view of 850 μm × 850 μm, and the total image is 3,400 μm × 3,400 μm. (Scale bar: 500 μm.) (*C*) A 3D reconstructed confocal image of a rhodamine-6G labeled 128-channel mesh electronics injected into water via a 400-μm ID needle (yellow dashed line). The image was acquired in 4 × 4 Tile Scan with each of the tile components having a field of view of 850 μm × 850 μm, and the total image size is 3,400 μm × 3,400 μm. The white arrow highlights the region of the mesh that is zoomed in and shown in *Inset* from a different viewing angle. (Scale bar: 500 μm.) (*Inset*) A magnified image of a single plane confocal image (3 μm focal depth) showing the four Au interconnect lines, which appear as dark lines, in each longitudinal mesh element (running upper left to lower right); in the upper right longitudinal element, yellow dashed lines highlight the positions of four Au interconnect lines. (Scale bar: 20 μm.) (*D*) Average impedance values between adjacent Au interconnects (2 μm edge-to-edge distance) on the same longitudinal elements of the 128-channel mesh design (red) and those of the Pt microelectrodes (20-μm diameter) of the same mesh probe measured in the frequency range of 1 kHz to 10 kHz. The averages were obtained over 10 pairs of adjacent Au interconnects and 10 Pt microelectrodes (*SI Text*). The shaded areas indicate ±1 SD with a sample size $N = 10$.

to use higher-resolution lithography to further increase the number of channels for this same basic design.

Multisite Injection and Interfacing Multiplexed Meshes for High-Density Recording. We first tested the significantly expanded mapping capability of the scalable multiplexed mesh electronics probes via controlled stereotaxic injection (32) of four probes into four distinct regions of the same mouse brain, as shown schematically in Fig. 4*A*. An important secondary advantage of this approach for multisite mapping is that the four flexible flat cables (FFCs) electrically connected to each of the implanted mesh electronics probes can be stacked on top of the mouse skull to provide a lightweight and low-profile interface for recording instrumentation.

A photograph taken following implantation of four 32-channel mesh electronics probes in a mouse (Fig. 4*B*; see *Materials and Methods* and *SI Text*) highlights the four injection holes with well-defined stereotaxic coordinates drilled bilaterally on top of the motor cortex (CTX, yellow arrows 1 and 2) and somatosensory CTX/hippocampus (HIP, yellow arrows 3 and 4) with the nonimplanted I/O portion of each mesh electronics probe unfolded onto one of the four FFCs (upper right quadrant, Fig. 4*B*). Microcomputed tomography (micro-CT) of the mouse following completion of the surgical procedure (Fig. 4*C*) confirms the extended morphologies of the four injected mesh electronics probes, and shows the four FFCs bonded at the top (dorsal, "D") of the skull. A photograph of an independent live mouse that underwent the same procedure to implant four 32-channel mesh electronics probes (Fig. 4*D*) further highlights the low-profile folded FFC instrumentation interface, which has a mass of ~0.15 g per FFC. The low profile and low mass of the instrumentation interface minimize interference with normal behavior of the mouse.

Stable Long-Term 128-Channel Brain Activity Mapping. We have tested the capabilities of the scalable mesh electronics probes through simultaneous 128-channel chronic recording from four 32-channel mesh electronics probes. The four mesh electronics probes were stereotaxically injected into the motor CTX (meshes 1 and 2) and HIP (meshes 3 and 4) of both hemispheres and electrically connected to four FFCs as described in *Multisite Injection and Interfacing Multiplexed Meshes for High-Density Recording* (see *Materials and Methods* and *SI Text*). During the entire course of our 4-mo chronic experiments, the mesh probe positions remained fixed (i.e., were not adjusted postinjection) to provide the strongest test of the stability of the mesh electronics/brain tissue interface. Representative LFP recordings from the four mesh electronics probes at 2 and 4 mo postinjection (Fig. S2*A*) show that LFPs with modulation amplitudes of ~300 μV were obtained from the 122/128 electrically connected channels, and that the LFPs recorded from mesh probes in the motor CTX (1 and 2, right and left hemispheres) and HIP (3 and 4, right and left hemispheres) demonstrate distinct temporal characteristics. Specifically, LFPs recorded from the motor CTX were dominated by relatively slow oscillations with a frequency characteristic of the prominent delta wave (1 Hz to 4 Hz) in the CTX (12, 42) (Fig. S2*A*). In contrast, LFPs recorded from the HIP exhibit a weaker delta wave and stronger faster oscillation representative of theta wave (4 Hz to 8 Hz) (41). These observed differences in relative strength of delta and theta waves in the HIP are consistent with literature reports (12, 41). In addition, comparison of the cross-channel correlation maps for the LFP data

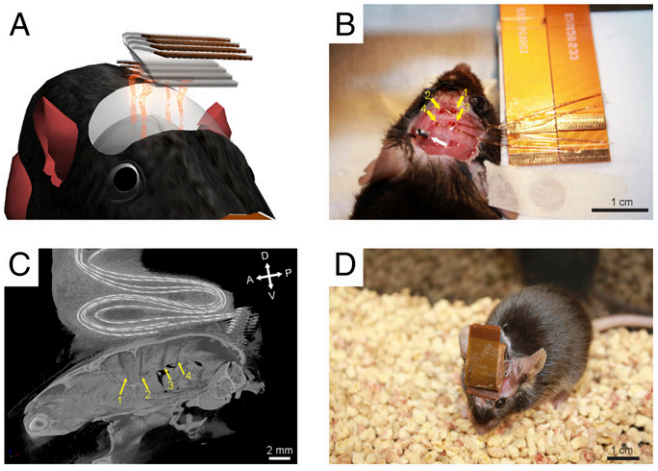

Fig. 4. Multisite injections of mesh electronics. (*A*) Schematic, (*B*) photo, and (*C*) micro-CT image showing four mesh electronics (yellow arrows) injected into the same mouse. Four FFCs were stacked both vertically and horizontally for I/O connections during surgery. A, P, D, and V in *C* correspond to the anterior, posterior, dorsal, and ventral directions, respectively. (*D*) Photo of a freely behaving mouse with four meshes injected. (Scale bars: 1 cm in *B* and *D*; 2 mm in *C*.)

recorded at 2 and 4 mo (Fig. S2*B*) showed similar patterns, suggesting that the four 32-channel mesh electrodes have stable interfaces/integration with the CTX and HIP neural tissue.

A more rigorous test of the stability of the multisite 128-channel recordings, which is central to the potential uniqueness of this work, is stable tracking of large numbers of single neurons. Representative extracellular action potential spikes recorded with the 128 channels from an awake mouse at 2 and 4 mo postinjection are shown in Fig. 5*A*. Overall, these data show relatively stable characteristic extracellular action potentials from the four mesh probes with spike amplitudes of ~50 μV to 200 μV over the 2-mo duration of these recordings. To assess quantitatively the chronic recording stability of the recorded single-unit spikes, we performed systematic analyses of the spike amplitudes, signal-to-noise rations (SNRs), firing rates, and sorted spikes at 2 and 4 mo postinjection (see *Materials and Methods* and *SI Text*). First, calculation of the average peak-to-peak spike amplitudes of the 122/128 electrically connected channels at 2 and 4 mo postinjection (Fig. 5*B*) shows that the majority of recording channels exhibit stable amplitudes from 2 mo to 4 mo postinjection. Specifically, 86 out of 109 channels with recorded spikes show <20% variation in average spike amplitude across this 2-mo period. In addition, analyses of the SNR for all of these recording channels (Fig. 5*B*) show all channels with sorted spikes exhibit an SNR > 4, and 67 channels present SNR > 8 at both 2 mo and 4 mo postinjection, excluding the possibility that the observed spikes were due to electrical noise. Furthermore, 72 out of 109 channels with sorted spikes show <20% variation in SNR across this 2-mo period, which confirms the stability of our probe–brain interface. Second, analyses of the average firing rate of each channel (Fig. 5*C*), which reflects the intrinsic biophysical activity of the recorded neurons (33, 42), show consistent values for 84 out of 109 channels with <5 Hz change in average firing rate over the 2-mo period.

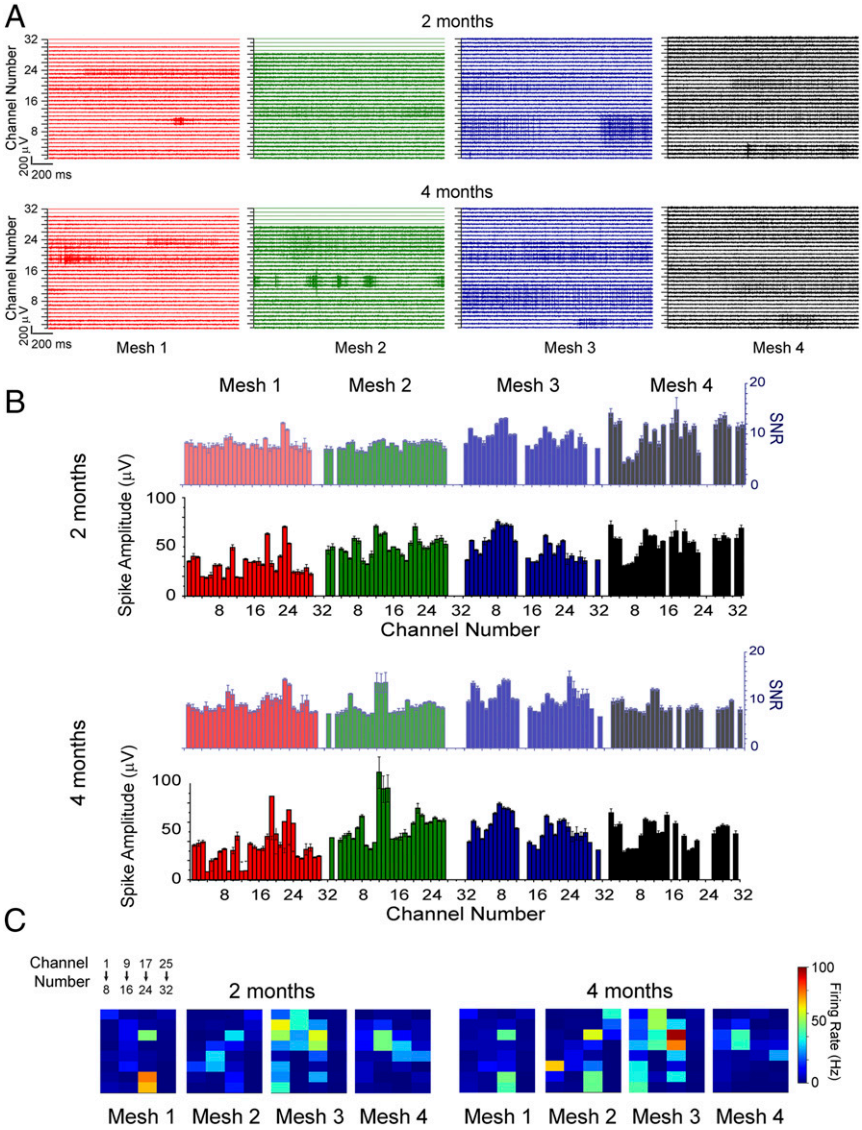

Fig. 5. Simultaneous 128-channel chronic recordings. (*A*) Band-pass (250 Hz to 6,000 Hz) filtered extracellular spike recordings from four 32-channel meshes injected into the same mouse at 2 (*Upper*) and 4 (*Lower*) mo postinjection. Meshes 1 (red) and 2 (green) were injected into the motor CTX, and meshes 3 (blue) and 4 (black) were injected into the HIP. (*B*) Bar charts showing average SNR (lighter colors, right *y* axis) and spike amplitude (darker colors, left *y* axis) from all channels at 2 (first and second rows) and 4 (third and fourth rows) mo postinjection. The color codes of different meshes are consistent with those in *A*. The error bars indicate the SEM, with sample size *N* equal to the total number of sorted spikes of the corresponding channel. See *SI Text* for details of SNR estimation. (*C*) Average firing rate maps of all channels at 2 (*Left*) and 4 (*Right*) mo postinjection. Colors indicate firing rate based on the color bar on the right.

Third, comparison of sorted spikes from meshes 1 and 3 (Fig. 6), which are representative of signals recorded from the HIP and CTX, respectively, provide particularly compelling evidence about the large-scale single-neuron recording stability of the implanted mesh electronics probes. Overall, these data exhibited consistent amplitudes and numbers of distinct neurons at 2 and 4 mo postinjection. For example, analyses of mesh 1 (Fig. 6*A*) demonstrate that 23 of the 28 channels show consistent spike waveforms and number of distinct clusters from 2 mo to 4 mo, while 4 out of 28 show the appearance of one neuron (channels 4, 18, 20, and 22) and 1 out of 28 shows appearance of two neurons (channel 30). Similarly, for mesh 3 (Fig. 6*B*), 23 out of 28 channels with sortable single-unit spikes exhibit identical clustering of spike waveforms from 2 mo to 4 mo postinjection. The other five channels showed either appearance or disappearance of one cluster between these two time points. The small variations in single neurons detected in 5 out of 28 channels for meshes 1 and 3 could reflect local brain tissue remodeling or, more probably, physiologically relevant circuit evolution with changes in synaptic strengths whose implications require further study. Together, these quantitative analyses demonstrate the capability of the highly multiplexed mesh electronics probes not only to track large populations of neurons but to do so with single-neuron-level long-term stability on at least a multimonth time scale. Last, we note that these new results are consistent with the absence of a chronic immune response and seamless integration of the mesh electronics with neural tissue determined from previous immunohistology studies of implanted mesh probes (33, 34) and confirmed by analyses with the scalable mesh electronics probes (Fig. S3).

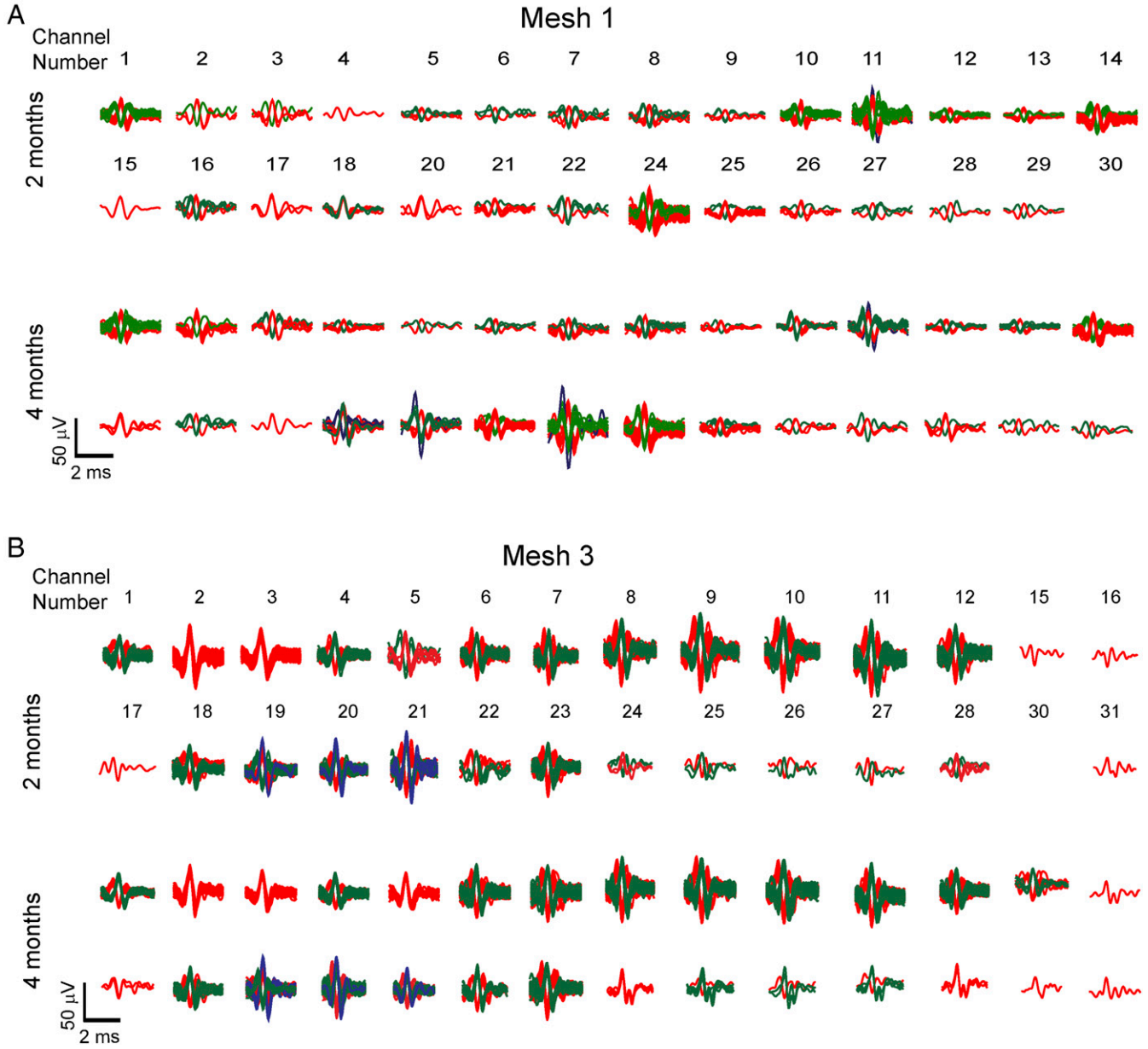

Fig. 6. Spike sorting analyses of chronic recordings. Overlay of sorted and clustered spikes from all channels with identifiable spikes for (*A*) mesh 1 and (*B*) mesh 3 in Fig. 5 at 2 mo (*Upper*) and 4 mo (*Lower*) postinjection. The channel numbers are specified above the corresponding sorted spikes for 2 mo and remain the same for 4 mo.

Multiplexed Chronic Recording from Freely Behaving Mice. We have also explored the capability of these highly multiplexed scalable mesh electronics probes for stable chronic electrophysiology measurements from freely behaving mice using a custom-designed printed circuit board (PCB) affixed to the mouse skull during implantation surgery (Fig. 7*A*). In short, a trimmed 32-channel FFC was electrically connected with the I/O of an injected 32-channel mesh electronics probe, and then inserted into a zero insertion force (ZIF) connector mounted on one side of the PCB. An amplifier connector on the other side of the PCB enabled plug-and-play recording with the signal amplifier and external recording instrument (Fig. 6*B*; see *Materials and Methods* and *SI Text* for details). The mesh electronics–FFC–PCB electrical interface has a total weight of only 1.3 g (0.65 g without the amplifier), imposing minimal interference on mice behavior whether they were housed in cages without the amplifier plugged in (Fig. 7*A*) or undergoing electrophysiological recordings with the amplifier (Fig. 7*B* and Movie S2).

Representative data and analyses of 32-channel chronic recordings obtained while a mouse was freely exploring a novel cage environment at 2 and 4 mo post stereotaxic injection such that both the HIP and primary somatosensory CTX were targeted with recording electrodes (see *Materials and Methods* and *SI Text*) highlight several points. First, low-pass filtered recording data yielded well-defined LFPs with modulation amplitudes of ∼300 μV in 32 out of 32 channels (heat maps, Fig. 7*C* and Fig. S4*A*). The LFPs from all channels showed stable amplitudes without signal degradation across this 2-mo period. In addition, cross-channel correlation maps of the LFP data (*Materials and Methods* and *SI Text*), which are indicative of cross-regional neuron ensemble synchronization and integration (14, 43), show similar patterns at 2 and 4 mo postinjection (Fig. S4*C*, *I* for both 2 and 4 mo).

Second, the similarity of single-unit extracellular action potentials observed from 26 out of 32 channels (black traces, Fig. 7*C* and Fig. S4*B*) at 2 and 4 mo postinjection suggests stability of

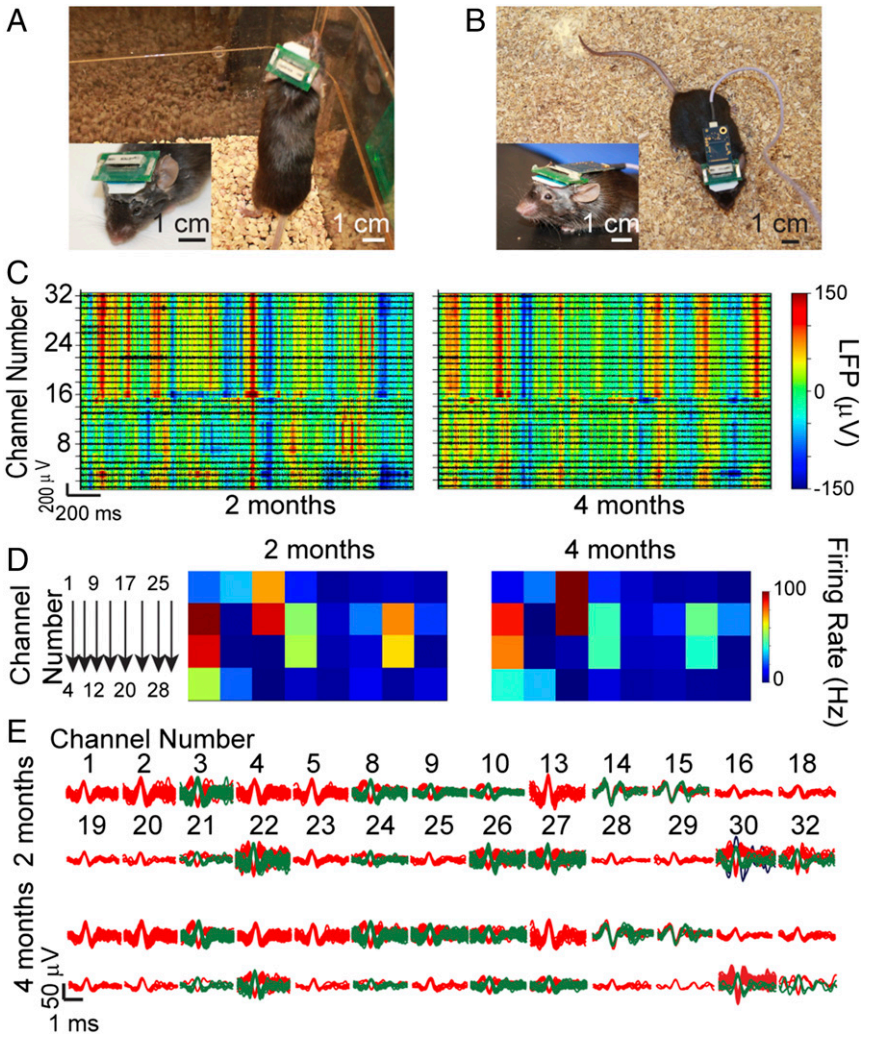

Fig. 7. Chronic recordings from freely behaving mouse. (*A*) Photograph of a typical freely behaving mouse with low-profile FFC and PCB when housed in animal facility. (*B*) Photograph of typical freely behaving mouse during recording. Voltage amplifier was directly positioned near the mouse head to minimize mechanical noise coupling. A flexible serial peripheral interface cable (light purple) was used to transmit amplified signals to the data acquisition systems. (*Insets*) Zoom-in views of the electrical connections on mouse head. (Scale bars: 1 cm.) (*C*) Representative 32-channel LFP (heat maps) with amplitudes color-coded according to the color bar on the far right and extracellular spikes (traces) mapping from the same mouse at 2 (*Left*) and 4 (*Right*) mo postinjection. The *x* axes show the recording time, and the *y* axes represent the channel number of each recording electrode. (*D*) Average spike firing rate maps of all channels at 2 (*Left*) and 4 (*Right*) mo postinjection. The channel numbers are specified on the left. Colors indicate firing rate based on the color bar on the right. (*E*) Sorted spikes from all 26 channels with identifiable spikes at 2 (first and second rows) or 4 (third and fourth rows) mo postinjection for recordings in *C*. The channel numbers are specified above the corresponding sorted spikes for 2 mo and remain the same for spikes recorded at 4 mo.

the single-unit recordings for this extended time period. Cross-channel correlation maps of the single-unit spikes (Fig. S4*C*, *II* for both 2 and 4 mo), which are indicative of cross-regional neuronal interactions and circuit topology (42), show similar patterns at 2 and 4 mo postinjection and thus support single-unit recording stability. In addition, comparison of the average firing rate of each channel from the 2- and 4-mo data (Fig. 7*D*) shows consistent values for the majority of the channels with <10 Hz change in average firing rate, indicating that the intrinsic biophysical activities of these recorded neurons are unchanged (33, 42).

Third, comparison of sorted spikes at 2 and 4 mo postinjection (Fig. 7*E*) demonstrates consistency both for spikes amplitudes and for number of distinct neurons recorded: 25 out of the 26 channels with sortable extracellular action potentials show both consistent spike amplitudes and number of distinct neurons recorded, while only one channel (channel 30) displays the disappearance of one neuron, possibly due to local neural circuit evolution over time. Together, these data strongly suggest that our scalable mesh electronics probes can also provide stable electrical recordings of neural networks down to the single-neuron level, with a high level of multiplexing over at least 2 mo from freely behaving mice.

Discussion

A scalable scheme for highly multiplexed mesh electronics probes with 32 to 128 recording channels per probe that also maintain the unique brain-like structure and mechanics of mesh was successfully implemented (Figs. 1–3). This scalable design combined with multisite injections was used to demonstrate functional mapping of interconnected brain regions with a low-profile and light-weight interface compatible with natural mouse behavior (Fig. 4). Studies with four 32-channel mesh probes injected into the motor CTX and HIP of the same mouse demonstrated simultaneous stable 128-channel long-term recordings of LFPs and single-unit extracellular spikes with stable single-neuron tracking up to at least 4 mo postinjection (Figs. 5 and 6 and Fig. S2). Last, we showed that the scalable mesh probes were capable of chronically monitoring a freely behaving mouse, where stable recording of interconnected neural networks down to the single-neuron level was achieved for at least 2 mo (Fig. 7 and Fig. S4).

The advances shown with the scalable mesh electronics probes can be compared with other existing neurotechnologies in several ways. First, compared with conventional rigid implantable devices, such as silicon probes and microwires, the 128-channel mesh design demonstrated in this work matches or even surpasses the achievable number and density of many of these probes (17–19), although more advanced fabrication has led to higher number and density in several reported silicon probes (23–25) (Harris TD, et al. Neuroscience Meeting Planner, November 12–16, 2016, San Diego, CA). Importantly, the ultra-flexible scalable mesh electronics probes show stable recordings over at least 2 mo compared with signal degradation on typically days to weeks time scale for these more rigid probes due to relative micromotion, neuron depletion, and chronic gliosis (26–30). Given that previous studies of much lower channel number mesh electronics have shown that stable recordings can be associated with a minimal chronic immune response (33, 34), it is reasonable to attribute this same origin for the stable-long term recordings achieved by these scalable mesh designs. In addition, while there are publications showing that conventional rigid probes occasionally report long-term stable chronic recording from a small portion (typically <10%) of the implanted electrodes (44), these results are more of an exception, as many researchers using the same type of probes reported intraday instability (28). Our present highly multiplexed mesh electronics probes demonstrate stable months-long recordings from the same neurons for the majority of the implanted electrodes with single-unit spikes detected.

Compared with recently developed flexible electrical probes, such as ultrasmall carbon (45), glass fiber (46), and polymer-based (39, 47) probes, which have exhibited reduced chronic immune response and longer recording stability versus conventional rigid probes, the compatibility of mesh electronics manufacturing with standard microfabrication procedures offers advantages in scalability of recording electrodes with well-defined spatial distributions. The seamless integration of the mesh electronics with brain tissue (34) has also been challenging to achieve with reported flexible probes (39, 45–47). Taken together, our highly multiplexed scalable mesh electronics probes bridge the gap between chronic stability, a key limitation to conventional rigid implantable devices, and channel scalability, a major challenge faced by recently developed flexible probes, by combining the advantages of existing neural probes in terms of ease of scalable microfabrication for high-density neuronal mapping, while outperforming other neurotechnologies by introducing a paradigm—the brain-like mesh electronics design—that affords chronically stable single-neuron recording.

The advance we demonstrate with these scalable highly multiplexed mesh electronics probes does not represent the limit of what is achievable with this approach. First, the incorporation of multiple interconnects into a single longitudinal element effectively transformed each longitudinal mesh element from a single-channel microwire-like probe to a multichannel Michigan-array-like unit. The use of standard microfabrication-based manufacturing, the insignificant contributions of interconnects to overall probe mechanics and recording impedance, and the minimum electrical cross-talk between adjacent channels all open substantial opportunity for further increasing the density and number of recording channels by defining narrower metal interconnects with smaller spacing. Indeed, state-of-the-art lithography can easily achieve sub-100-nm and even sub-10-nm patterning (48), which could yield 10- to 100-fold increase of interconnect density compared with our current design. We also envision that this approach could benefit from implementation of a "plug-and-play" type of I/O connection that would be more compatible with standard parallel microelectronics interfacing (49). Second, mechanical engineering of the scalable mesh electronics to enable the use of smaller-diameter needles and smaller volumes of liquid for injection could further increase the number of meshes that are implanted into relatively small rodent brains. This would also reduce the extent of disruption introduced during initial injection process and facilitate more rapid integration with the neural network. Third, incorporation of different functional capabilities, such as electrical and optical modulation (33, 50) as well as chemical and mechanical sensing (36–38, 51), could provide additional information relating to the coordination and interplay of, for example, action potentials and neural modulatory molecules, both of which are important to brain function.

We stress, however, that the unique capability to record from a large population of neurons across multiple brain regions with long-term stability at the single-neuron level demonstrated in this work already opens up new opportunities in neuroscience, including mapping the formation and evolution of neuronal circuits involved in learning, subsequent tracking of memory engrams at time points long after encoding, and elucidation of the neuronal basis of cognitive functions and processes in constant adaptation to a dynamic environment and aging (21, 52, 53). In addition, the capability to interface and interact with the same targeted neural circuits and pathways with single-neuron resolution could greatly facilitate the development of BMIs by obviating the need for constant adjustment of decoding algorithms (8–10).

Materials and Methods

Design and Fabrication of Syringe-Injectable Electronics. The highly multiplexed mesh electronics used a fabrication procedure similar to our recent reports (31–35). Key steps and mesh parameters are overviewed in Fig. S1 and described in *SI Text*. In brief, (*i*) a sacrificial layer of Ni was thermally

evaporated (Sharon Vacuum) onto a 3-inch Si wafer (Nova Electronic Materials); (*ii*) negative photoresist SU-8 (MicroChem Corp.) was spin-coated on the Si wafer and then patterned by PL with a mask aligner (ABM mask aligner); (*iii*) the wafer was then spin-coated with positive photoresist Shipley 1805 (The Dow Chemical Company), which was then was patterned by PL; (*iv*) a 1.5-nm-thick Cr layer and a 100-nm-thick Au layer were sequentially deposited by electron beam evaporation (Denton Vacuum) to make the Au interconnect lines; (*vi*) steps *iii* and *iv* were repeated for PL patterning and deposition of Pt electrodes (Cr: 1.5 nm, Pt: 50 nm); (*vii*) step *ii* was repeated for PL patterning of the top SU-8 layer; and, (*viii*) subsequently, the Si wafer was transferred to a Ni etchant solution to release the mesh electronics from the Si substrate. Released mesh electronics were rinsed with deionized (DI) water, and transferred to an aqueous solution of 1× PBS (Thermo Fisher Scientific Inc.) before use.

Mechanical Simulations. We estimated the bending stiffness of the mesh electronics with different structures using finite element software ABAQUS as described previously (31). A unit cell similar to figure 1d in ref. 31 was used for the simulation, where the mesh electronics were modeled with shell elements: A homogeneous single shell section with 800-nm-thick SU-8 was assigned to the transverse elements; a composite section with three layers of 400-nm-thick SU-8, 100-nm-thick gold, and another 400-nm-thick SU-8 was assigned to the longitudinal elements. Both SU-8 and gold are modeled as linear elastic materials, with Young's moduli of 2 and 79 GPa, respectively (31). The effective bending stiffness per width of planar polyimide, per width of silicon probes, and per diameter of microwire probes were estimated using standard formulae (54) with probe parameters including Young's moduli and probe dimensions based on literature reports (18, 39, 40). The effective bending stiffness per width of brain tissue was estimated based on similar formulae (54) with reported Young's modulus range (55). More details of the bending stiffness calculations are described in *SI Text*.

Mesh Electronics Imaging. Wide-field images with bright-field illumination were recorded using an Olympus BX51 microscope (Olympus). Confocal fluorescence microscopy and DIC images were recorded using a Zeiss LSM 880 confocal microscope (Carl Zeiss Microscopy). Confocal images were acquired under 10× magnification using a 561-nm-wavelength laser to excite mesh electronics labeled with rhodamine-6G fluorescent dye with a 1 Airy Unit (AU) pinhole. More details of the imaging conditions are described in *SI Text*.

Electrical Characterization. Impedance measurements in Fig. 3*D* were carried out using an Agilent B1500A semiconductor device parameter analyzer (Agilent Technologies Inc.) with B1520A-FG multifrequency capacitance measurement unit in the frequency range of 1 kHz to 10 kHz.

In Vivo Mouse Survival Surgery. Key steps for stereotaxic surgery and injection of mesh electronics into the brains of live mice are similar to our recent reports (31–34) and are described in *SI Text*. In brief, all tools and mesh electronics probes were sterilized before use. Anesthetized mice (adult male C57BL/6J mice; Jackson Laboratory) were placed in the stereotaxic frame (Lab Standard Stereotaxic Instrument; Stoelting Co.) to perform surgery, controlled injection, and electrical connection. All procedures performed on the mice were approved by the Animal Care and Use Committee of Harvard University. The animal care and use programs at Harvard University meet the requirements of the federal law (89-544 and 91-579), and National Institutes of Health (NIH) regulations and are also accredited by the American Association for Accreditation of Laboratory Animal Care (AAALAC).

Micro-CT. One mouse injected with four mesh electronics probes was euthanized and decapitated following the guidelines approved by the Animal Care and Use Committee of Harvard University, which meet the requirements of the Federal Law (89-544 and 91-579) and NIH regulations and are also accredited by American Association for Accreditation of Laboratory Animal Care (AAALAC). The decapitated mouse head was imaged using an HMXST Micro-CT X-ray scanning system with a standard horizontal imaging axis cabinet (model HMXST225; Nikon Metrology, Inc.). Imaging parameters were set as 95 kV and 93 μA for scanning. Before scanning, shading correction and flux normalization were applied to adjust the X-ray detector. The CT Pro-3D software (ver. 2.2; Nikon-Metris) was used to calibrate centers of rotation for micro-CT sinograms and to reconstruct all 2D images. VGStudio MAX software (ver. 2.2; Volume Graphics GMbh) was used for 3D rendering and analysis of the reconstructed images.

In Vivo Chronic Brain Recording in Mice. Mice with implanted and electrically connected mesh electronics (four 32-channel mesh electronics for the 128-channel recordings or one 32-channel mesh for recordings from freely behaving mice) were recorded chronically on a biweekly basis. Mice were restrained in a Tailveiner restrainer (Braintree Scientific LLC) or were freely roaming in a novel cage for restrained or freely behaving recordings, respectively. The 0-80 set screw was used as a reference. Electrophysiological recording was made using an Intan evaluation system (Intan Technologies LLC) with a 20-kHz sampling rate and a 60-Hz notch filter. More details of the electrical recordings are described in *SI Text*.

Analysis of Electrophysiological Recording Data. The electrophysiological recording data were analyzed offline, with details described in *SI Text*. In brief, raw recording data were filtered using noncausal Butterworth band-pass filters ("filtfilt" function in Matlab) in the 250- to 6,000-Hz frequency range to extract single-unit spikes (33), and in the 0.1- to 150-Hz range to extract LFP (33). The correlation coefficient maps of LFPs and single-unit spike recording traces were calculated based on the standard Pearson product-moment correlation coefficient for time series. Single-unit spike sorting was performed by amplitude thresholding, and then clustered to determine the number of recorded single neurons using the WaveClus software. Spikes assigned to the same cluster were coded with the same color.

ACKNOWLEDGMENTS. We thank J. Huang for help with recording instrumentation, T. G. Schuhmann and J. Yao for help with fabrication, and X. Yang for helpful discussions. This work was funded by the Air Force Office of Scientific Research (FA9550-14-1-0136), Harvard University Physical Sciences and Engineering Accelerator award, and National Institute on Drug Abuse of the National Institutes of Health (1R21DA043985-01). G.H. was supported by an American Heart Association Postdoctoral Fellowship (16POST27250219) and a Pathway to Independence Award from The National Institute on Aging of the National Institutes of Health (1k99AG056636). This work was performed, in part, at the Harvard University Center for Nanoscale Systems, a member of the National Nanotechnology Coordinated Infrastructure Network, which is supported by the National Science Foundation.

1. Buzsáki G (2004) Large-scale recording of neuronal ensembles. *Nat Neurosci* 7: 446–451.
2. Stanley GB (2013) Reading and writing the neural code. *Nat Neurosci* 16:259–263.
3. Bargmann CI, Newsome WT (2014) The Brain Research through Advancing Innovative Neurotechnologies (BRAIN) initiative and neurology. *JAMA Neurol* 71:675–676.
4. Harris KD, Quiroga RQ, Freeman J, Smith SL (2016) Improving data quality in neuronal population recordings. *Nat Neurosci* 19:1165–1174.
5. Borchers S, Himmelbach M, Logothetis N, Karnath HO (2011) Direct electrical stimulation of human cortex—The gold standard for mapping brain functions? *Nat Rev Neurosci* 13:63–70.
6. Lozano AM, Lipsman N (2013) Probing and regulating dysfunctional circuits using deep brain stimulation. *Neuron* 77:406–424.
7. Cash SS, Hochberg LR (2015) The emergence of single neurons in clinical neurology. *Neuron* 86:79–91.
8. Shenoy KV, Carmena JM (2014) Combining decoder design and neural adaptation in brain-machine interfaces. *Neuron* 84:665–680.
9. Bensmaia SJ, Miller LE (2014) Restoring sensorimotor function through intracortical interfaces: Progress and looming challenges. *Nat Rev Neurosci* 15:313–325.
10. Lebedev MA, Nicolelis MAL (2017) Brain-machine interfaces: From basic science to neuroprostheses and neurorehabilitation. *Physiol Rev* 97:767–837.
11. Choi S, Lee H, Ghaffari R, Hyeon T, Kim D-H (2016) Recent advances in flexible and strechable bio-electronic devices integrated with nanomaterials. *Adv Mater* 28: 4203–4218.
12. Buzsáki G, Anastassiou CA, Koch C (2012) The origin of extracellular fields and currents–EEG, ECoG, LFP and spikes. *Nat Rev Neurosci* 13:407–420.
13. Kim D-H, et al. (2010) Dissolvable films of silk fibroin for ultrathin conformal bio-integrated electronics. *Nat Mater* 9:511–517.
14. Poldrack RA, Farah MJ (2015) Progress and challenges in probing the human brain. *Nature* 526:371–379.
15. Lin MZ, Schnitzer MJ (2016) Genetically encoded indicators of neuronal activity. *Nat Neurosci* 19:1142–1153.
16. Ji N, Freeman J, Smith SL (2016) Technologies for imaging neural activity in large volumes. *Nat Neurosci* 19:1154–1164.
17. Berényi A, et al. (2014) Large-scale, high-density (up to 512 channels) recording of local circuits in behaving animals. *J Neurophysiol* 111:1132–1149.
18. Schwarz DA, et al. (2014) Chronic, wireless recordings of large-scale brain activity in freely moving rhesus monkeys. *Nat Methods* 11:670–676.
19. Shobe JL, Claar LD, Parhami S, Bakhurin KI, Masmanidis SC (2015) Brain activity mapping at multiple scales with silicon microprobes containing 1,024 electrodes. *J Neurophysiol* 114:2043–2052.

20. Samanez-Larkin GR, Knutson B (2015) Decision making in the ageing brain: Changes in affective and motivational circuits. *Nat Rev Neurosci* 16:278–289.
21. Josselyn SA, Köhler S, Frankland PW (2015) Finding the engram. *Nat Rev Neurosci* 16: 521–534.
22. Okubo TS, Mackevicius EL, Payne HL, Lynch GF, Fee MS (2015) Growth and splitting of neural sequences in songbird vocal development. *Nature* 528:352–357.
23. Yamamoto J, Wilson MA (2008) Large-scale chronically implantable precision motorized microdrive array for freely behaving animals. *J Neurophysiol* 100:2430–2440.
24. Scholvin J, et al. (2016) Close-packed silicon microelectrodes for scalable spatially oversampled neural recording. *IEEE Trans Biomed Eng* 63:120–130.
25. Lopez CM, et al. (2016) A 966-electrode neural probe with 384 configurable channels in 0.13 μm SOI CMOS. IEEE International Solid-State Circuits Conference (ISSCC) (Inst Electr Electron Eng, New York), pp 392–393.
26. Polikov VS, Tresco PA, Reichert WM (2005) Response of brain tissue to chronically implanted neural electrodes. *J Neurosci Methods* 148:1–18.
27. Karumbaiah L, et al. (2013) Relationship between intracortical electrode design and chronic recording function. *Biomaterials* 34:8061–8074.
28. Perge JA, et al. (2013) Intra-day signal instabilities affect decoding performance in an intracortical neural interface system. *J Neural Eng* 10:036004.
29. Lacour SP, Courtine G, Guck J (2016) Materials and technologies for soft implantable neuroprostheses. *Nat Rev Mater* 1:16063.
30. Chen R, Canales A, Anikeeva P (2017) Neural recording and modulation technologies. *Nat Rev Mater* 2:16093.
31. Liu J, et al. (2015) Syringe-injectable electronics. *Nat Nanotechnol* 10:629–636.
32. Hong G, et al. (2015) Syringe injectable electronics: Precise targeted delivery with quantitative input/output connectivity. *Nano Lett* 15:6979–6984.
33. Fu T-M, et al. (2016) Stable long-term chronic brain mapping at the single-neuron level. *Nat Methods* 13:875–882.
34. Zhou T, et al. (2017) Syringe-injectable mesh electronics integrate seamlessly with minimal chronic immune response in the brain. *Proc Natl Acad Sci USA* 114: 5894–5899.
35. Xie C, et al. (2015) Three-dimensional macroporous nanoelectronic networks as minimally invasive brain probes. *Nat Mater* 14:1286–1292.
36. Tian B, et al. (2012) Macroporous nanowire nanoelectronic scaffolds for synthetic tissues. *Nat Mater* 11:986–994.
37. Liu J, et al. (2013) Multifunctional three-dimensional macroporous nanoelectronic networks for smart materials. *Proc Natl Acad Sci USA* 110:6694–6699.
38. Feiner R, et al. (2016) Engineered hybrid cardiac patches with multifunctional electronics for online monitoring and regulation of tissue function. *Nat Mater* 15: 679–685.
39. Rousche PJ, et al. (2001) Flexible polyimide-based intracortical electrode arrays with bioactive capability. *IEEE Trans Biomed Eng* 48:361–371.
40. Lee H, Bellamkonda RV, Sun W, Levenston ME (2005) Biomechanical analysis of silicon microelectrode-induced strain in the brain. *J Neural Eng* 2:81–89.
41. Buzsáki G (2002) Theta oscillations in the hippocampus. *Neuron* 33:325–340.
42. Shadlen MN, Newsome WT (1998) The variable discharge of cortical neurons: Implications for connectivity, computation, and information coding. *J Neurosci* 18:3870–3896.
43. Varela F, Lachaux J-P, Rodriguez E, Martinerie J (2001) The brainweb: Phase synchronization and large-scale integration. *Nat Rev Neurosci* 2:229–239.
44. Vaidya M, et al. (2014) Ultra-long term stability of single units using chronically implanted multielectrode arrays. *Conf Proc IEEE Eng Med Biol Soc* 2014:4872–4875.
45. Kozai TD, et al. (2012) Ultrasmall implantable composite microelectrodes with bioactive surfaces for chronic neural interfaces. *Nat Mater* 11:1065–1073.
46. Canales A, et al. (2015) Multifunctional fibers for simultaneous optical, electrical and chemical interrogation of neural circuits in vivo. *Nat Biotechnol* 33:277–284.
47. Luan L, et al. (2017) Ultraflexible nanoelectronic probes form reliable, glial scar-free neural integration. *Sci Adv* 3:e1601966.
48. Päivänranta B, Langner A, Kirk E, David C, Ekinci Y (2011) Sub-10 nm patterning using EUV interference lithography. *Nanotechnology* 22:375302.
49. Schuhmann TG, Jr, Yao J, Hong G, Fu T-M, Lieber CM (2017) Syringe-injectable electronics with a plug-and-play input/output interface. *Nano Lett* 17:5836–5842.
50. Jiang Y, et al. (2016) Heterogeneous silicon mesostructures for lipid-supported bioelectric interfaces. *Nat Mater* 15:1023–1030.
51. Hanson L, et al. (2015) Vertical nanopillars for in situ probing of nuclear mechanics in adherent cells. *Nat Nanotechnol* 10:554–562.
52. Holtmaat A, Caroni P (2016) Functional and structural underpinnings of neuronal assembly formation in learning. *Nat Neurosci* 19:1553–1562.
53. Wang M, et al. (2011) Neuronal basis of age-related working memory decline. *Nature* 476:210–213.
54. Steif PS (2012) *Mechanics of Materials* (Pearson, New York).
55. Tyler WJ (2012) The mechanobiology of brain function. *Nat Rev Neurosci* 13:867–878.
56. Paxinos G, Franklin KB (2001) *The Mouse Brain in Seterotaxic Coordinates* (Academic, New York), 2nd Ed.
57. Quiroga RQ, Nadasdy Z, Ben-Shaul Y (2004) Unsupervised spike detection and sorting with wavelets and superparamagnetic clustering. *Neural Comput* 16:1661–1687.